Ultrafast Synthesis of Transition Metal Phosphides in Air via Pulsed Laser Shock

Ziyuan Xu,[‖,†] Qiao Chen,[‖,†] Xiao Han,[‖,†,§,⊥,] Jiaxuan Wang,[†] Pan Wang,[†] Tao Zheng,[†] Sin-Yi Pang,[⊥] Jincheng Wang,[†] Hejun Li,[†] Zhenhai Xia,[‡] Jianhua Hao[⊥,*]*

[†]*State Key Laboratory of Solidification Processing, School of Materials Science and Engineering, Northwestern Polytechnical University, Xi'an, 710072, PR China*

[§]*Chongqing Innovation Center, Northwestern Polytechnical University, Chongqing, PR China*

[⊥]*Department of Applied Physics, The Hong Kong Polytechnic University, Hong Kong, PR China*

[‡]*School of Chemical Engineering, University of New South Wales, Sydney NSW, 2052 Australia*

[*]*Email: xiao.han@nwpu.edu.cn (X. Han)*

jh.hao@polyu.edu.hk (J. Hao)

[‖]*These authors contributed equally to this work.*

Abstract

Transition metal phosphide nanoparticles (TMP NPs) represent a promising class of nanomaterials in the field of energy; however, a universal, time-saving, energy-efficient, and scalable synthesis method is currently lacking. Here, a facile synthesis approach is firstly introduced using a pulsed laser shock (PLS) process mediated by metal-organic frameworks, free of any inert gas protection, enabling the synthesis of diverse TMP NPs. Additionally, through thermodynamic calculations and experimental validation, the phase selection and competition behavior between phosphorus and oxygen have been elucidated, dictated by the redox potential and electronegativity. The resulting composites exhibit balanced performance and extended durability. When employed as electrocatalysts for overall water splitting, as-constructed electrolyzer achieves a low cell voltage of 1.54 V at a current density of 10 mA cm^{-2}. This laser method for phosphides synthesis provides clear guidelines and holds potential for the preparation of nanomaterials applicable in catalysis, energy storage, biosensors, and other fields.

Introduction

Transition metal phosphide nanoparticles are of interest in a wide range of applications, including thermal catalysis and electrocatalysis, energy storage, and biosensing/imaging[1–3]. To develop TMP NPs with well-performed properties, deploying organic/inorganic barriers or overlayers recently appears to be one of the favorable countermeasures, which promises to reconcile high activity with improved stability of compound entities[4,5]. Metal-organic frameworks (MOFs), a type of organic-inorganic hybrid material with regular porous structures and tunable compositions, have been demonstrated as efficient sacrificial templates and precursors for preparing a series of carbon and transition metal compound nanoparticles (TMC NPs)[6–8], including transition metal oxides (TMOs)[9,10], phosphides (TMPs)[11,12], and oxyphosphides (TMOPs)[13,14].

To date, most MOF-derived TMP NPs/C nanomaterials have been synthesized through a two-step pyrolysis routine[15–17]. Carbonization of MOF precursors and incorporation of extraneous anions are included, which are cost- and time-consuming[18]. Moreover, on account of mechanical damage caused by the long-term thermal treatment process, immobilizing TMP NPs/C composites to temperature-sensitive metallic substrates (i.e., metal foam) while maintaining their mechanical stability is a daunting task. Therefore, breakthroughs and new synthetic methods based on controllable, cost-effective, and space-limited pyrolysis of MOFs are urgently needed for preparing TMP NPs/C with adjustable composition, selected phase, and desired catalytic performance.

Several instant heating techniques like joule thermal shock[19,20], microwave-assisted heating[21,22], flame synthesis[23,24] and laser manufacturing[25,26], recently emerge as time- and cost-effective approaches to replace conventional furnace carbonization. Among them, laser scribing technique demonstrates its industrial potential in terms of precision, patterning, compatibility and high-scalability[27]. Especially, pulsed CO_2 laser provided by the commercial laser cutter could induce instantaneously local high temperature to break interatomic bonding and *in situ* produce a reducing atmosphere, which performs as a promising tool to manipulate the synthesis of various nanostructures[28–30]. However, due to the stringent synthesis conditions of TMPs,

reports of TMP NPs synthesized through laser or other rapid synthesis methods are still lacking[31,32].

Herein, a time- and power-efficient PLS method to fabricate MOF-derived core-shell structures with nanosized TMP NPs encapsulated in graphitic carbon is reported. By combining laser radiation technology and the chemistry of MOFs, the structure and composition of TMP NPs/C can be precisely controlled. The PLS strategy employs an ultrahigh local temperature and ultrafast heating/cooling rate, thus inducing the fast pyrolysis and recrystallization of MOF precursors without causing thermal damage on conductive support. In addition, the PLS process could be completed within several minutes with several watts of energy consumption, and the strategy here could be extended to synthesize different MOF derivatives.

Results and discussions

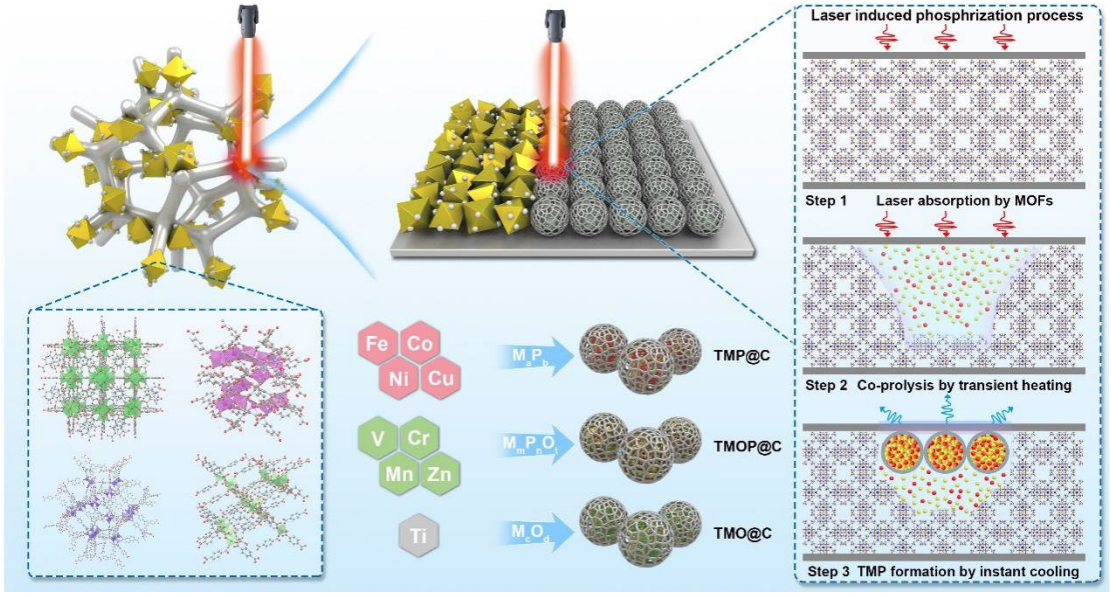

Figure 1. Schematic illustration of the synthesis process of MOF-derived transitional metal phosphide nanoparticles on nickel foam via a pulsed laser shock strategy.

Figure 1 presents a schematic diagram illustrating the synthesis of LIP-MOFs (LIP: Laser-Induced Phosphorization) on a three-dimensional conductive substrate, specifically nickel foam (NF) or carbon cloth (CC), via the PLS strategy. A variety of MOFs, incorporating different metal ions, were synthesized through a solvothermal method. These include ZIF-8 (Zn), HKUST-1 (Cu), Ni-BTC (Ni), ZIF-67 (Co), Co-BDC (Co), MIL-101 (Fe), Mn-BDC (Mn), MIL-101 (Cr), MIL-47 (V), and MIL-125 (Ti). The organic linkers employed were chosen based on the specific metal elements, with BDC (Ti, V, Cr, Mn, Fe, Co), BTC (Ni, Cu), DHTA (Zn), and 2-MeIm (Co), as detailed in Table S1.

Following the preloading of MOFs and phosphorus source onto NF, the PLS process was utilized to convert these precursors into TMC NPs/C heterostructures, referred to LIP-MOFs. The laser parameters are detailed in Figure S1. Comprehensive characterization techniques were employed to analyze their structure and composition. Figure S2 presents the PXRD patterns of several synthesized representative MOFs, demonstrating a high degree of overlap with the ideal MOF crystal structures. SEM

images of LIP-MOFs (Figure S2) indicated that post-laser irradiation, the different MOF precursors transformed into similar three-dimensional cross-linked porous composites. Enlarged SEM images (Figure S4-S12) revealed these composite carbon structures uniformly and firmly adhered to the nickel foam framework, forming a multiscale porous cross-linked structure.

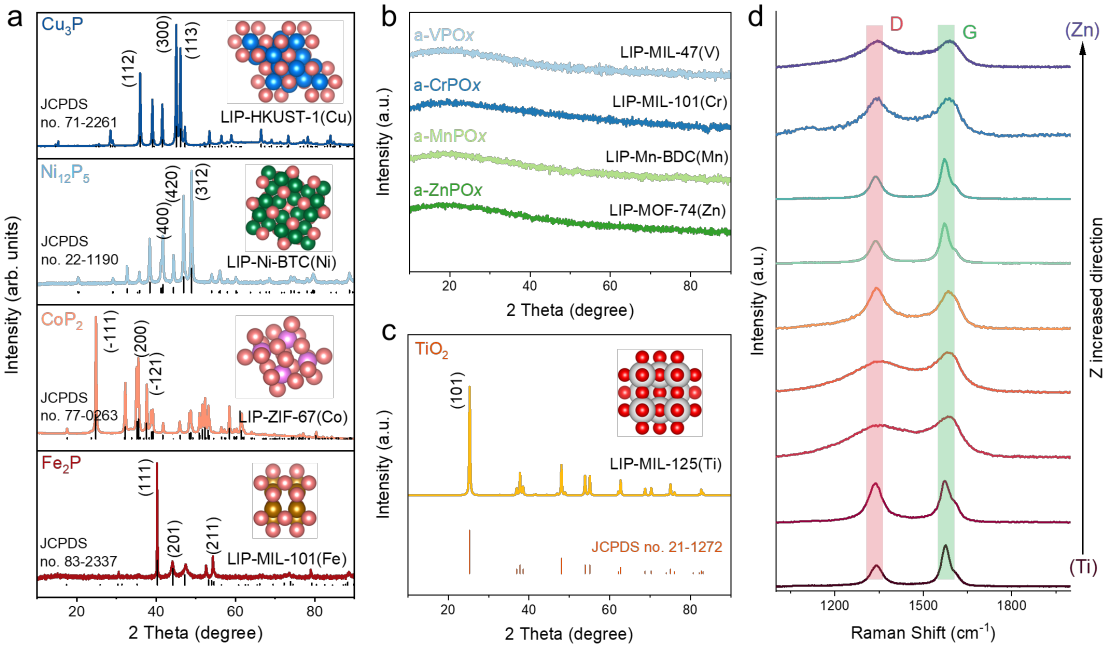

Figure 2. Structural Evolution Analysis of MOFs under Pulse Laser Shock. a, PXRD patterns of TMP NPs (TM = Fe, Co, Ni, Cu). **b,** PXRD patterns of TMOPs (TM = V, Cr, Mn, Zn), **c,** PXRD patterns of TMO NPs (TM = Ti). **d,** Raman spectra of LIP-MOFs.

Through PXRD analysis, it was observed that the phase structures after LIP predominantly fall into three categories: (i) crystalline phosphides for Fe, Co, Ni, and Cu (Figure 2a); (ii) amorphous oxyphosphides for V, Cr, Mn, and Zn (Figure 2b); and (iii) crystalline oxides for Ti (Figure 2c). The PXRD results indicate that not all metals consistently yield phosphide phases under identical laser irradiation conditions. The intrinsic formation mechanisms of these three major products will be further discussed in subsequent sections.

In the process of laser-induced synthesis of TMP nanoparticles, the photothermal effect

induced by laser triggers localized transient high temperatures in the irradiated area[28,33], promoting the carbonization of MOF precursors. During this carbonization, the organic linkers and anion sources generate a localized reducing atmosphere, including H_2, CH_4, C_2H_4, and CO[34,35]. Subsequently, phosphorization occurs with PH_3 produced from the thermal decomposition of sodium hypophosphite, ultimately resulting in the formation of TMP NPs.

In addition to the transformation of metal centers, the Raman spectra in Figure 2d also verify the conversion of organic linkers into graphene structures, which provides robust support for TMP nanoparticles. Although the crystalline/defect degree of graphene is influenced by the intrinsic characteristics of the MOF types, it does not vary with the metal centers. Additionally, during the PLS process, a systematic evolution of the product crystal phase was observed with increasing atomic number, transitioning from oxides to oxyphosphides, and subsequently to phosphides. However, this trend does not hold for the element Zn, as depicted in Figure S13. This deviation presents a challenge to developing guiding principles for the selective synthesis of phosphides under PLS conditions.

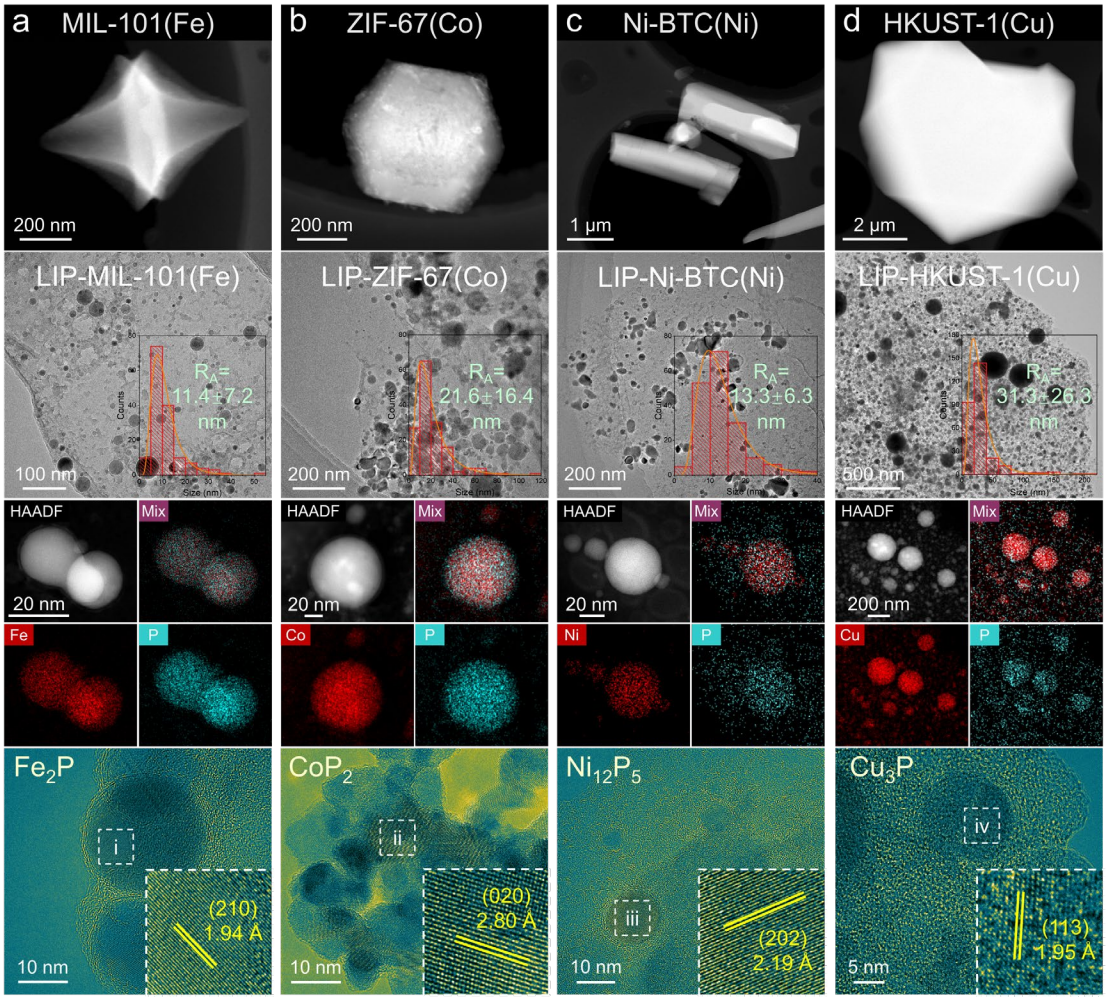

Figure 3. General synthesis of various transition-metal phosphides (including iron, cobalt, nickel, and copper) via the PLS strategy. a-d, TEM characterizations, including BF, HAADF, EDS element mapping, HRTEM images and corresponding IFFT patterns of (**a**) LIP-MIL-101(Fe), (**b**) LIP-ZIF-67(Co), (**c**) LIP-Ni-BTC(Ni), (**d**) LIP-HKUST-1(Cu) and their corresponding MOF precursors. The insets are size distribution plots.

Cs-TEM was employed to characterize the morphology and structural features of LIP-MOF at a more microscopic scale. As shown in Figures 3a-3d, four types of MOF precursors and their laser-irradiated derivatives were studied. TEM images prior to PLS processing indicated that the synthesized MOFs exhibited regular polyhedral morphologies, which transformed into loaded nanoparticles post-PLS processing. The four types of LIP-MOFs (MIL-101(Fe), ZIF-67(Co), Ni-BTC(Ni), and HKUST-1(Cu)) demonstrated similar characteristics at the micro/nano scale, featuring uniformly

dispersed spherical nanoparticles enveloped by ultra-thin carbon layers. Notably, despite undergoing the same PLS process, different TMP NPs exhibited distinct size distributions. The average size (R_A) followed the order: $Fe_2P < Ni_{12}P_5 < CoP_2 < Cu_3P$, correlating with the varying thermal diffusion capabilities of the respective metals.

HAADF and corresponding EDS images confirmed the homogeneous distribution of phosphorus and the corresponding metal elements (Fe, Co, Ni, Cu) in the TMP nanoparticles. In addition to the PXRD results (Figure 2a), HRTEM and SAED provided nanoscale structural information, clearly demonstrating the successful synthesis of TMP nanoparticles via PLS treatment (Figure 3 and S14). Although the P/M ratio in the precursor was fixed, the resulting phosphides exhibited different P/M ratios within the range of (1/3, 2), encompassing phosphorus-deficient phases (Fe_2P, $Ni_{12}P_5$, and Cu_3P) and phosphorus-rich phases (CoP_2). This variation may be attributed to the higher thermodynamic stability of these phases under PLS conditions[36].

The ultrafine size of the TMP nanoparticles can be attributed to the transient high temperatures and ultrafast heating and cooling rates induced by pulse laser irradiation, which prevent Ostwald ripening processes[37,38]. As the heated region affected by laser irradiation is only at the micro/nano scale[39], atomic diffusion effects are limited, allowing the reduction atmosphere generated in situ to protect TMP from environmental oxidation without the need for additional inert gas as protective agent. These advantages enable our PLS strategy to synthesize ultrafine TMP nanoparticles with high phase purity.

Although Fe, Co, Ni, and Cu tend to form TMP NPs under PLS conditions, two other types of nanomaterials were also observed: amorphous structures based on V, Cr, Mn, and Zn, and oxides based on Ti. TEM results (Figure S15) showed that the corresponding MOF precursors had specific shapes, which transformed into irregular carbonaceous composites after PLS treatment. Unlike the uniformly distributed nanoparticle morphology of TMP NPs/C on the carbon support, the LIP-MOFs (M = V, Cr, Mn, and Zn) exhibit a homogeneous distribution of metal, phosphorus, and oxygen elements, but lack the uniformly loaded nanoparticles. The uniform distribution of P/O/metals and high O content in the carbonaceous matrix indicated a well-mixed state

of elements in the amorphous TMOP phase. By conducting comparative experiments to adjust the ratio of the metal source to the phosphorus source in the precursor (Tables S2-S3), the broadly tunable Cr/P ratio in the LIP-MIL-101(Cr) was demonstrated, thereby confirming its oxyphosphide structure. Additionally, no obvious lattice fringes were observed in HRTEM images, and the SAED patterns exhibited typical characteristics of amorphous phases, consistent with the PXRD results (Figure 2b).

Combining composition and structural analysis confirmed the structure of amorphous TMOPs, including a-VPO_X, a-$CrPO_X$, a-$MnPO_X$, and a-$ZnPO_X$. Interestingly, unlike the impurities in TMP NPs, nickel species evaporated from the NF substrate (T_{max} = 2200 K > nickel melting point = 1728 K, Figure S16) were present as separated nickel-based phosphide nanoparticles in TMOP/C composites. HRTEM (Figure S17a-S17c, S17f-S17g), HAADF-EDS elemental analysis (Figure S17d) and PXRD pattern (Figure S18) verified the presence of crystalline $Ni_{12}P_5$ in four LIP-MOFs (M = V, Cr, Mn, and Zn) when using NF as supporter. Additionally, TEM results (Figure S19-S20) indicated that the NPs in LIP-MIL-125(Ti) were determined to be TiO_2 doped with phosphorus in a tetragonal crystal structure, consistent with the PXRD results. EPR spectra (Figure S21) showed a signal peak around g = 2.001 can be attributed to unpaired electrons trapped by oxygen vacancies, suggesting a higher oxygen vacancies concentration induced by P doping in TiO_2 nanocrystals from LIP-MIL-125(Ti).

Thermodynamic calculations and validation experiments were conducted to study the phase selection behavior of LIP-MOFs. Considering the system's exposure to a complex environment containing both P and O, studying the competitive reactions between oxidation and phosphorization was crucial (Figure 4a). Three typical reactions were summarized as follows: R1: $M(C_xH_yO_z) + P \rightarrow M_aP_b$, R2: $M(C_xH_yO_z) + O \rightarrow M_cO_d$, and R3: $M(C_xH_yO_z) + P + O \rightarrow M_mP_nO_t$. It was evident that the selectivity of metal elements towards oxidation and phosphorization was critical in determining whether TMP NPs could be successfully synthesized during the PLS process[40].

Different metals exhibit varying oxidation potentials $\Delta G_{Oxidation}$, indicating the difficulty of reducing their oxides to the metallic state. This oxidation potential quantifies the metal's affinity for oxygen[41]. Thermodynamic calculations are extensively employed

to predict equilibrium positions within systems, typically neglecting intermediate states. As depicted in Figure 4b, the Ellingham diagram, based on these thermodynamic calculations, reveals the $\Delta G_{Oxidation}$ and corresponding reduction difficulty for the selected metals' oxides[42].

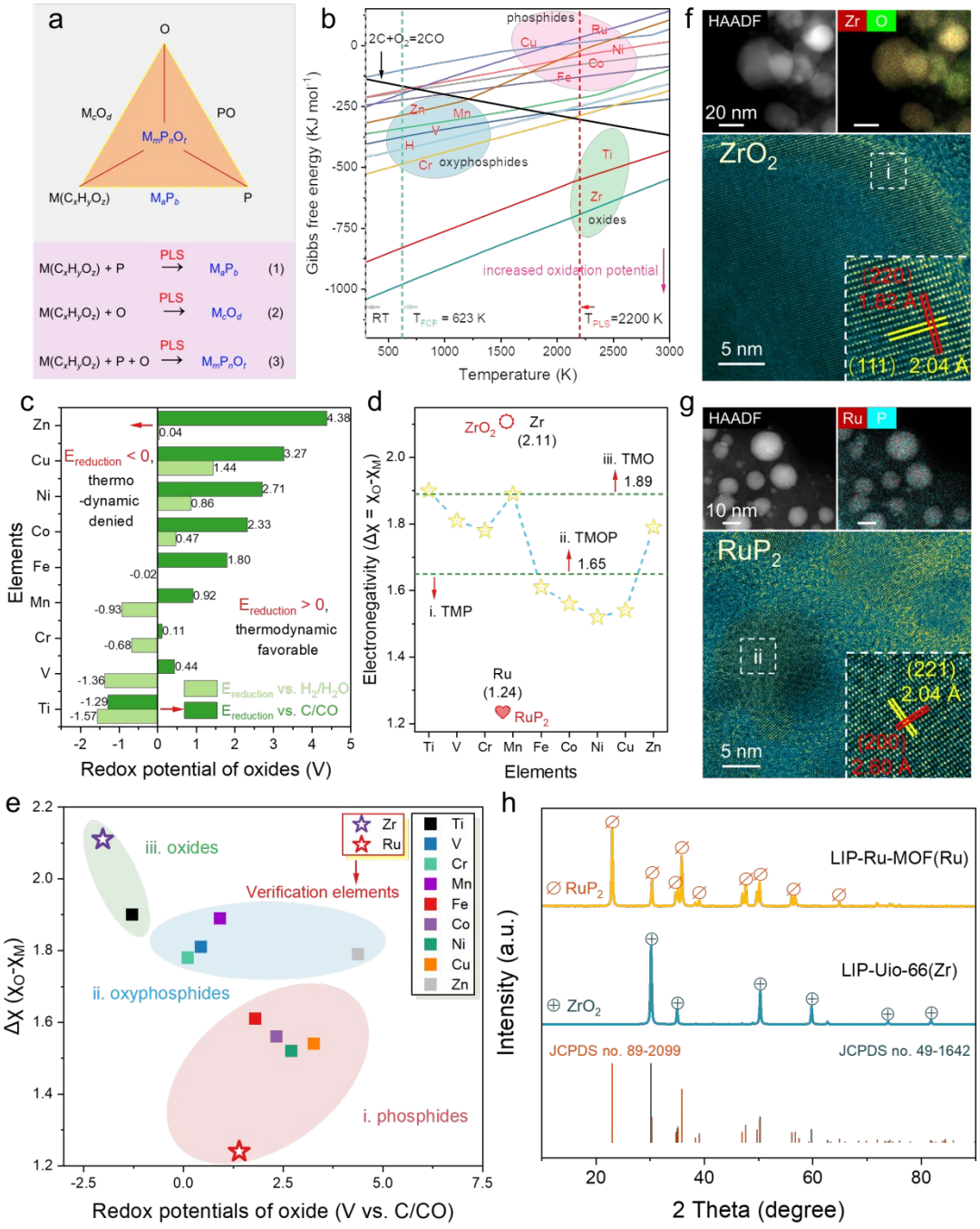

Figure 4. Thermodynamic studies on phase selectivity during the PLS process. a, Growth phase diagrams of transition metal-based M_aP_b, M_cO_d, and $M_mP_nO_t$. **b,** Ellingham diagram (bulk materials, 1 atm O_2 partial pressure). **c,** Electrochemical redox

potentials of selective metal oxides (vs. C/CO and vs. H_2/H_2O). **d,** Electronegativity (χ) deviation between oxygen and selected metal elements. **e,** Discriminant analysis of obtained phases using electronegativity and redox potentials. Validation test results. **f, g,** TEM Results, Including HAADF-EDS and HRTEM Images of **(f)** LIP-UiO-66(Zr) and **(g)** LIP-Ru-MOF(Ru). **h,** PXRD Patterns.

Generally, the elements within the red circle, including Fe, Ni, Co, Cu, and Zn, demonstrate lower levels of oxidation potential, while elements within the blue circle, such as Ti, V, Cr, and Mn, exhibit higher oxidation potentials. This trend aligns well with the phase selectivity between transition metal phosphides, oxyphosphides, and oxides under PLS conditions, although there are exceptions (e.g., Zn). Notably, carbon is commonly used as a high-temperature reducing agent, capable of reducing elements located above the carbon-oxide line (the black line in Figure 4b) through carbothermal reduction. The Ellingham diagram serves as a preliminary guide to the oxidation potentials of different elements.

The ability of various reducing agents to donate electrons to the metal elements within the precursors can be approximated by their electrochemical redox potentials in metal oxides[43]. Thermodynamic energy calculations for different oxides were conducted (Figure S22) to evaluate their respective redox potentials ($E_{\text{Reduction}}$) relative to different reducing agents, as illustrated in Figure 4c (vs. H_2/H_2O and vs. C/CO). For instance, the redox potential for the Cr^{3+}/Cr couple at 2200 K is 0.11 V and -0.68 V relative to C/CO and H_2/H_2O, respectively. Consequently, the carbothermal reduction from oxidized Cr to metallic Cr is a spontaneous process, whereas the redox reaction between H_2 and Cr_2O_3 requires additional energy input. Based on the calculated $E_{\text{Reduction}}$ values, the reaction $MO_n + nC = M + nCO\ (g)$ is generally more thermodynamically favorable within this system than the reaction $MO_n + nH_2\ (g) = M + nH_2O\ (g)$. Therefore, the $E_{\text{Reduction}}$ vs. C/CO (carbothermal reduction potential) was determined to be the descriptor for metal oxidation behavior. As shown in Figure S23, there is a good match between the obtained phases and the $E_{\text{Reduction}}$ vs. C/CO except Zn. According to the carbothermal reduction potential criterion, MOF-74(Zn) should yield zinc phosphide

under laser irradiation, but instead, it forms zinc oxyphosphides, indicating that $E_{Reduction}$ vs. C/CO alone cannot accurately predict the final phase structure.

Figure 4d elucidates a discernible correlation between the deviation in M-O electronegativity and the resultant phases. Among the selected transition metals, Fe, Co, Ni, and Cu exhibit higher electronegativity values (as depicted in Figure S24), whereas Ti, V, Cr, Mn, and Zn manifest lower values. Generally, metals with diminished electronegativity signify a propensity towards oxygen affinity[44], thereby designating Ti, V, Cr, Mn, and Zn as potent deoxidizers[45]. Typically, as summarized in Figure 4e, transition metals characterized by low $E_{Reduction}$ and heightened electronegativity tend to yield crystalline phosphides. This observation implies that the intrinsic attributes of the central metal (carbothermal reduction potential and electronegativity) can reliably prognosticate the phase and composition of TMP NPs/C, offering a fundamental design guideline.

To corroborate the predictability of the established criteria, we selected two additional d-block elements from beyond the first transition series (Zr and Ru) for validation. In accordance with the discriminant analysis outlined in Figure 4e, Zr exhibits a high carbothermal reduction potential ($E_{Reduction}$ vs. C/CO = -2.02 V) alongside a low electronegativity (χ = 1.33), while Ru shows a low carbothermal reduction potential ($E_{Reduction}$ vs. C/CO = 1.40 V) and high electronegativity (χ = 2.2). Consequently, UiO-66(Zr) and Ru-MOF(Ru) are anticipated to undergo transformation into zirconium-based oxide and ruthenium-based phosphide, respectively, following PLS treatment. Subsequent analysis, as delineated in TEM results (Figures 4f-4g and Figures S25-S26) and PXRD patterns (Figure 4h), confirms the phase compositions as cubic ZrO_2 and marcasite-type RuP_2, respectively, in meticulous accordance with the prediction. This empirical validation underscores the accuracy and reliability of the phase selection criteria established within this study.

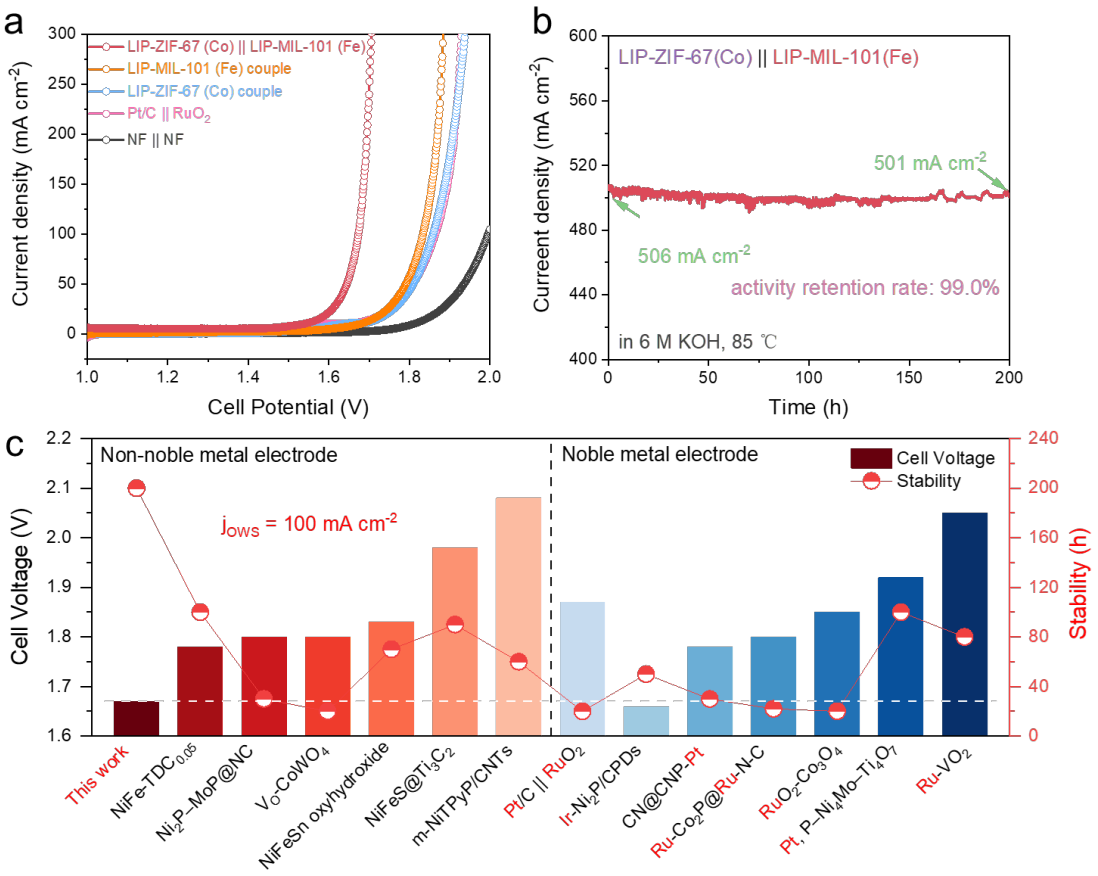

Figure 5. Overall water splitting performance of LIP-MOFs. a, LSV curves collected using a two-electrode water splitting system. **b,** Stability testing via the amperometric *i-t* technique under a simulated industrial water splitting environment (6 M KOH, 85°C). **c,** Performance and stability contrast to reported advanced water electrolysis systems.

Transition metal phosphide catalysts derived from MOFs typically demonstrate remarkable electrocatalytic performance in water splitting due to their efficient charge injection and transfer to active sites[46–48]. In both the hydrogen evolution reaction (HER) and the oxygen evolution reaction (OER), LIP-MOFs exhibited superior electrocatalytic activity. To be specific, LIP-ZIF-67(Co) showed HER activity comparable to that of commercial Pt/C catalysts at high current densities, with overpotentials of 115 mV and 190 mV at current densities of 10 mA cm^{-2} and 100 mA cm^{-2}, respectively (Figures S27). The OER, being a four-electron transfer process, requires more activation energy than its corresponding cathodic reaction, emphasizing

the importance of identifying superior OER catalysts[49]. As illustrated in Figures S28, LIP-MIL-101(Fe) achieved current densities of 10 mA cm^{-2} and 100 mA cm^{-2} with remarkably low overpotentials of 201 mV and 232 mV, respectively, surpassing other LIP-MOFs electrodes and RuO_2@NF (313 mV and 375 mV), as well as other reported advanced electrocatalysts (Table S5). The intrinsic activity of LIP-MOFs was evaluated by calculating the electrochemical double-layer capacitance and turnover frequency values (Figure S29-S31). The LIP-MIL-101(Fe) and LIP-ZIF-67(Co) demonstrated highest intrinsic activity towards OER and HER, respectively.

These LIP-MOFs catalysts were utilized as cathode and anode to construct an electrolyzer for overall water splitting (OWS) experiments. Compared to other LIP-MOF counterparts and commercial catalysts, the configuration of LIP-ZIF-67(Co) as cathode and LIP-MIL-101(Fe) as anode exhibited the highest activity during OWS. As depicted in Figure 5a, the electrolyzer required voltages of 1.54 V and 1.67 V to achieve 10 mA cm^{-2} and 100 mA cm^{-2}, respectively. This performance surpasses most recent literature reports (Table S6), indicating significantly enhanced catalytic activity. Regarding long-term stability (Figure S32), the electrolyzer operated at approximately 680 mA cm^{-2} for over 110 hours without any decay, outperforming the Pt/C || RuO_2 counterpart.

To investigate the origin of the exceptional stability, we conducted various experiments to study their compositional and structural evolution behavior. Time-dependent ICP-OES measurements (Figure S33) indicated that the total leaching of Fe, Co, and P ions was minimal throughout the reaction (total leaching <1 ppm), and the leaching rates of all ions dropped to very low levels after 50 hours, which is consistent with their electrocatalytic stability. Post-reaction PXRD and TEM showed that the LIP-ZIF-67(Co) as cathode maintained its crystalline phase and nanoparticle morphology due to the protection of the encapsulating carbon structure (Figure S34-S35), while the LIP-MIL-101(Fe) as anode underwent reconstruction from Fe_2P nanoparticles into goethite α-FeOOH nanorod structures (Figure S36-S38). XPS results (Figure S39) indicate that Fe in Fe_2P exists in a high oxidation state, which may promote the spontaneous reconstruction of Fe_2P during the anodic OER process.

As illustrated in Figure S40, the configuration of LIP-ZIF-67(Co) || LIP-MIL-101(Fe) exhibited multifaceted potential across various electrolytes, and maintained outstanding stability over 200 hours at an industrial-level current density of 1.65 V under simulated harsh industrial conditions (Figure 5b), indicating its potential for industrial application. As depicted in Figure 5c, the electrolyzer demonstrates performance comparable to, or even surpassing, that of the most advanced transition metal/noble metal-based electrodes in alkaline water electrolyzers. This can be attributed to the confined ultra-rapid heating and cooling technique, which induces abundant defects (Figure S41-S42) within the nanocrystals while minimizing thermal radiation damage to the matrix material.

3. Conclusion

In conclusion, we have developed a facile, rapid, and energy-efficient PLS technique capable of synthesizing TMP NPs/porous carbon composites within seconds in ambient air. The concurrent pyrolysis of MOF precursors and anionic species facilitates the ultra-rapid recrystallization of carbon and the formation of TMPs. This PLS strategy's scalability and versatility were validated through the synthesis of various MOF-derived TMP NPs. Moreover, by integrating experimental results with theoretical analysis, we established a guideline based on electrochemical redox potential and electronegativity for predicting phase selection during the PLS process, providing a directive for subsequent TMP NPs synthesis via PLS. We demonstrate the application potential of TMP NPs/C composites towards water electrolysis system. The proposed PLS strategy enables the controlled and large-scale synthesis of TMP NPs/C on conductive substrates, guided by computational insights, and holds promise for a variety of applications, including electrocatalysis, adsorptive materials, and supercapacitors.

Acknowledgement

This work was funded by the National Natural Science Foundation of China (52472304, 52002324), Natural Science Foundation of Chongqing (cstc2021jcyj-msxmX0471), Hong Kong Scholars Program (XJ2021073, PolyU YZ4V), Hong Kong RGC GRF

(PolyU 15301121), PolyU grant (1-CE0H). We would like to thank the Analytical & Testing Center of Northwestern Polytechnical University for partial support on sample characterizations.

Supporting Information

Supplementary information is available in the online version of the paper.

Authors Information

Ziyuan Xu: School of Materials Science and Engineering, Northwestern Polytechnical University, Xi'an, 710072, PR China

Qiao Chen: School of Materials Science and Engineering, Northwestern Polytechnical University, Xi'an, 710072, PR China

Xiao Han: School of Materials Science and Engineering, Northwestern Polytechnical University, Xi'an, 710072, PR China; Chongqing Innovation Center, Northwestern Polytechnical University, Chongqing, 401135, PR China

Jiaxuan Wang: School of Materials Science and Engineering, Northwestern Polytechnical University, Xi'an, 710072, PR China

Pan Wang: School of Materials Science and Engineering, Northwestern Polytechnical University, Xi'an, 710072, PR China

Tao Zheng: School of Materials Science and Engineering, Northwestern Polytechnical University, Xi'an, 710072, PR China

Sin-Yi Pang: Department of Applied Physics, The Hong Kong Polytechnic University, Hong Kong, 999077, PR China

Jincheng Wang: School of Materials Science and Engineering, Northwestern Polytechnical University, Xi'an, 710072, PR China

Hejun Li: School of Materials Science and Engineering, Northwestern Polytechnical University, Xi'an, 710072, PR China

Zhenhai Xia: School of Chemical Engineering, University of New South Wales, Sydney, 2052, Australia

Jianhua Hao: Department of Applied Physics, The Hong Kong Polytechnic University, Hong Kong, 999077, PR China

Additional information

The authors declare no conflicts of interest.

Key words

pulsed laser shock, transition-metal phosphide nanoparticles, ultrafast synthesis, metal-organic frameworks, electrocatalysis

References

[1] S. H. Li, M. Y. Qi, Z. R. Tang, Y. J. Xu. Nanostructured metal phosphides: from controllable synthesis to sustainable catalysis. *Chem Soc Rev* **2021**, *50*, 7539.

[2] H. Teymourian, A. Barfidokht, J. Wang. Electrochemical glucose sensors in diabetes management: an updated review (2010–2020). *Chem Soc Rev* **2020**, *49*, 7671.

[3] Y. Yang, B. Sun, Z. Sun, J. Xue, J. He, Z. Wang, K. Sun, Z. Sun, H. K. Liu, S. X. Dou. Recent advances and strategies of metal phosphides for accelerating polysulfide redox and regulating Li plating. *Coord Chem Rev* **2024**, *510*, 215836.

[4] G. Li, Y. Feng, Y. Yang, X. Wu, X. Song, L. Tan. Recent advances in transition metal phosphide materials: Synthesis and applications in supercapacitors. *Nano Mater Sci* **2024**, *6*, 174.

[5] T. J. Wang, Y. C. Jiang, J. W. He, F. M. Li, Y. Ding, P. Chen, Y. Chen. Porous palladium phosphide nanotubes for formic acid electrooxidation. *Carbon Energy* **2022**, *4*, 283.

[6] X. Wang, G. Zhang, W. Yin, S. Zheng, Q. Kong, J. Tian, H. Pang. Metal–organic framework-derived phosphide nanomaterials for electrochemical applications. *Carbon Energy* **2022**, *4*, 246.

[7] Y. Qian, F. Zhang, S. Zhao, C. Bian, H. Mao, D. J. Kang, H. Pang. Recent progress of metal-organic framework-derived composites: Synthesis and their energy conversion applications. *Nano Energy* **2023**, *111*, 108415.

[8] R. Anne Acedera, A. Theresse Dumlao, D. J. Donn Matienzo, M. Divinagracia, J. Anne Paraggua, P. Y. Abel Chuang, J. Ocon. Templated synthesis of transition metal phosphide electrocatalysts for oxygen and hydrogen evolution reactions. *J Energy Chem* **2024**, *89*, 646.

[9] T. Wei, Y. Zhou, C. Sun, X. Guo, S. Xu, D. Chen, Y. Tang. An intermittent lithium deposition model based on CuMn-bimetallic MOF derivatives for composite lithium anode with ultrahigh areal capacity and current densities. *Nano Res* **2024**, *17*, 2763.

[10] G. Yang, Y. Jiao, H. Yan, Y. Xie, A. Wu, X. Dong, D. Guo, C. Tian, H. Fu. Interfacial engineering of MoO_2-FeP heterojunction for highly efficient hydrogen evolution coupled with biomass electrooxidation. *Adv Mater* **2020**, *32*, 202000455.

[11] H. Liu, S. Yang, J. Ma, M. Dou, F. Wang. Surface engineering of MOFs as a route to

cobalt phosphide electrocatalysts for efficient oxygen evolution reaction. *Nano Energy* **2022**, *98*, 107315.

[12] H. Zhang, A. Chen, Z. Bi, X. Wang, X. Liu, Q. Kong, W. Zhang, L. Mai, G. Hu. MOF-on-MOF-derived ultrafine Fe_2P-Co_2P heterostructures for high-efficiency and durable anion exchange membrane water electrolyzers. *ACS Nano* **2023**, *17*, 24070.

[13] D. D. Babu, Y. Huang, G. Anandhababu, M. A. Ghausi, Y. Wang. Mixed-metal–organic framework self-template synthesis of porous hybrid oxyphosphides for efficient oxygen evolution reaction. *ACS Appl Mater Interfaces* **2017**, *9*, 38621.

[14] L. Yang, L. Zhang. Interfacial electronic modification of bimetallic oxyphosphides as multi-functional electrocatalyst for water splitting and urea electrolysis. *J Colloid Interface Sci* **2022**, *607*, 546.

[15] Y. Shi, M. Li, Y. Yu, B. Zhang. Recent advances in nanostructured transition metal phosphides: synthesis and energy-related applications. *Energy Environ Sci* **2020**, *13*, 4564.

[16] J. Su, J. Zhou, L. Wang, C. Liu, Y. Chen. Synthesis and application of transition metal phosphides as electrocatalyst for water splitting. *Sci Bull* **2017**, *62*, 633.

[17] J. Theerthagiri, A. P. Murthy, S. J. Lee, K. Karuppasamy, S. R. Arumugam, Y. Yu, M. M. Hanafiah, H. S. Kim, V. Mittal, M. Y. Choi. Recent progress on synthetic strategies and applications of transition metal phosphides in energy storage and conversion. *Ceram Int* **2021**, *47*, 4404.

[18] X. Cui, J. Chen, Z. Sun, L. Wang, Q. Peng, B. Xiao, L. Zhao, H. Zheng, Y. Wang, J. Wang, X. Chen, Q. Zhang, S. Chen. A general route for encapsulating monodispersed transition metal phosphides into carbon multi-chambers toward high-efficient lithium-ion storage with underlying mechanism exploration. *Adv Funct Mater* **2023**, *33*, 202212100.

[19] H. Wu, Q. Lu, Y. Li, J. Wang, Y. Li, R. Jiang, J. Zhang, X. Zheng, X. Han, N. Zhao, J. Li, Y. Deng, W. Hu. Rapid joule-heating synthesis for manufacturing high-entropy oxides as efficient electrocatalysts. *Nano Lett* **2022**, *22*, 6492.

[20] G. Li, W. Zhang, K. Nie, X. Lv, J. Deng, H. Ji. Flash Joule heating to enhance water oxidation of hematite photoanode via mediating with an oxidized carbon overlayer.

Carbon **2023**, *215*, 118444.

[21] Q. Li, J. Gao, X. Zang, C. Dai, H. Zhang, L. Xin, W. Jin, W. Xiao, G. Xu, Z. Wu, L. Wang. Synergistic effects of pyrrolic N/pyridinic N on ultrafast microwave synthesized porous CoP/Ni_2P to boost electrocatalytic hydrogen generation. *Inorg Chem* **2023**, *62*, 21508.

[22] Q. Li, X. Luan, Z. Xiao, W. Xiao, G. Xu, Z. Li, Z. Wu, L. Wang. Ultrafast microwave synthesis of Ru-doped MoP with abundant P vacancies as the electrocatalyst for hydrogen generation in a wide pH range. *Inorg Chem* **2023**, *62*, 9687.

[23] S. Park, D. Shin, T. Yeo, B. Seo, H. Hwang, J. Lee, W. Choi. Combustion-driven synthesis route for tunable TiO_2/RuO_2 hybrid composites as high-performance electrode materials for supercapacitors. *Chem Eng J* **2020**, *384*, 123269.

[24] D. Shin, H. Hwang, T. Yeo, S. Park, T. Kim, J. Lee, W. Choi. Sol-gel-driven combustion wave for scalable transformation of $Mn(NO_3)_2$ precursors into MnO_{2-x}/MWCNT supercapacitor electrodes capable of electrochemical activation. *Carbon* **2019**, *152*, 746.

[25] B. Pang, X. Liu, T. Liu, T. Chen, X. Shen, W. Zhang, S. Wang, T. Liu, D. Liu, T. Ding, Z. Liao, Y. Li, C. Liang, T. Yao. Laser-assisted high-performance PtRu alloy for pH-universal hydrogen evolution. *Energy Environ Sci* **2022**, *15*, 102.

[26] H. Lim, H. Kwon, H. Kang, J. E. Jang, H. J. Kwon. Structural isomers: small change with big difference in anion storage. *Nano-Micro Lett* **2024**, *16*, 13.

[27] X. Cui, Y. Liu, Y. Chen. Ultrafast micro/nano-manufacturing of metastable materials for energy. *Natl Sci Rev* **2024**, *11*, nwae033.

[28] W. Zhang, R. Li, H. Zheng, J. Bao, Y. Tang, K. Zhou. Laser-assisted printing of electrodes using metal–organic frameworks for micro-supercapacitors. *Adv Funct Mater* **2021**, *31*, 2009057.

[29] H. Jiang, S. Jin, C. Wang, R. Ma, Y. Song, M. Gao, X. Liu, A. Shen, G. J. Cheng, H. Deng. Nanoscale laser metallurgy and patterning in air using MOFs. *J Am Chem Soc* **2019**, *141*, 5481.

[30] Y. J. Tang, H. Zheng, Y. Wang, W. Zhang, K. Zhou. Laser-induced annealing of metal–organic frameworks on conductive substrates for electrochemical water splitting. *Adv Funct Mater* **2021**, *31*, 2102648.

[31] Q. Liu, S. W. Chen. Ultrafast synthesis of electrocatalysts. *Trends Chem* **2022**, *4*, 918.

[32] X. Hu, D. Zuo, S. Cheng, S. Chen, Y. Liu, W. Bao, S. Deng, S. J. Harris, J. Wan. Ultrafast materials synthesis and manufacturing techniques for emerging energy and environmental applications. *Chem Soc Rev* **2023**, *52*, 1103.

[33] Y. Wu, Z. Huang, H. Jiang, C. Wang, Y. Zhou, W. Shen, H. Xu, H. Deng. Facile synthesis of uniform metal carbide nanoparticles from metal–organic frameworks by laser metallurgy. *ACS Appl Mater Interfaces* **2019**, *11*, 44573.

[34] H. Hu, Q. Li, L. Li, X. Teng, Z. Feng, Y. Zhang, M. Wu, J. Qiu. Laser irradiation of electrode materials for energy storage and conversion. *Matter* **2020**, *3*, 95.

[35] W. Chen, R. V. Salvatierra, M. Ren, J. Chen, M. G. Stanford, J. M. Tour. Laser-induced silicon oxide for anode-free lithium metal batteries. *Adv Mater* **2020**, *32*, 2002850.

[36] I. A. Liyanage, A. V. Flores, E. G. Gillan. Tunable synthesis of metal-rich and phosphorus-rich nickel phosphides and their comparative evaluation as hydrogen evolution electrocatalysts. *Inorg Chem* **2023**, *62*, 4947.

[37] Y. Yao, Z. Huang, P. Xie, S. D. Lacey, R. J. Jacob, H. Xie, F. Chen, A. Nie, T. Pu, M. Rehwoldt, D. Yu, M. R. Zachariah, C. Wang, R. Shahbazian-Yassar, J. Li, L. Hu. Carbothermal shock synthesis of high-entropy-alloy nanoparticles. *Science*, **2018**, *359*, 1489.

[38] T. Hu, P. Li, W. Zhang, Y. Ye, J. Liu, Y. Cai, G. Zhang, K. Dai, C. Liang. Laser irradiation induced platinum-based bimetallic alloy nanoparticles in liquids for electrocatalytic hydrogen production. *J Alloys Compd* **2023**, *934*, 167914.

[39] H. Lim, H. Kwon, H. Kang, J. E. Jang, H. J. Kwon. Laser-induced and MOF-derived metal oxide/carbon composite for synergistically improved ethanol sensing at room temperature. *Nano-Micro Lett* **2024**, *16*, 113.

[40] F. Chen, B. Zhao, M. Sun, C. Liu, Y. Shi, Y. Yu, B. Zhang. Mechanistic insight into the controlled synthesis of metal phosphide catalysts from annealing of metal oxides with sodium hypophosphite. *Nano Res* **2022**, *15*, 10134.

[41] Y. Yao, Z. Huang, L. A. Hughes, J. Gao, T. Li, D. Morris, S. E. Zeltmann, B. H. Savitzky, C. Ophus, Y. Z. Finfrock, Q. Dong, M. Jiao, Y. Mao, M. Chi, P. Zhang, J. Li, A. M. Minor, R. Shahbazian-Yassar, L. Hu. Extreme mixing in nanoscale transition metal

alloys. *Matter* **2021**, *4*, 2340.

[42] D. Van Lam, M. Sohail, V. T. Nguyen, Q. T. Ngo, A. Anto Jeffery, H. S. Choi, N. Jung, J. H. Kim, H. Kim, S. M. Lee. Laser-scribed ultrasmall nanoparticles with unary and binary phases. *Chem Eng J* **2021**, *421*, 127731.

[43] Y. Li, H. Shao, Z. Lin, J. Lu, L. Liu, B. Duployer, P. O. Å. Persson, P. Eklund, L. Hultman, M. Li, K. Chen, X. H. Zha, S. Du, P. Rozier, Z. Chai, E. Raymundo-Piñero, P. L. Taberna, P. Simon, Q. Huang. A general Lewis acidic etching route for preparing MXenes with enhanced electrochemical performance in non-aqueous electrolyte. *Nat Mater* **2020**, *19*, 894.

[44] R. G. Parr, L. V. Szentpály, S. Liu. Electrophilicity Index. *J Am Chem Soc* **1999**, *121*, 1922.

[45] L. Han, H. Cheng, W. Liu, H. Li, P. Ou, R. Lin, H. T. Wang, C. W. Pao, A. R. Head, C. H. Wang, X. Tong, C. J. Sun, W. F. Pong, J. Luo, J. C. Zheng, H. L. Xin. A single-atom library for guided monometallic and concentration-complex multimetallic designs. *Nat Mater* **2022**, *21*, 681.

[46] K. Jang, H. Yoon, J. S. Hyoung, D. S. A. Pratama, C. W. Lee, D. W. Kim. Enhancement of hydrogen evolution activity by tailoring the electronic structure in ruthenium-heteroatom-doped cobalt iron phosphide nanoframes. *Appl Catal B* **2024**, *341*, 123327.

[47] Z. M. Wang, Q. L. Hong, X. H. Wang, H. Huang, C. Yu, S. N. Li. RuP nanoparticles anchored on N-doped graphene aerogels for hydrazine oxidation-boosted hydrogen production. *Acta Physico-Chimica Sinica* **2023**, 39, 2303028.

[48] L. Quan, H. Jiang, G. Mei, Y. Sun, B. You. Bifunctional electrocatalysts for overall and hybrid water splitting. *Chem Rev* **2024**, *124*, 3694.

[49] J. Zhang, H. Bin Yang, D. Zhou, B. Liu. Adsorption energy in oxygen electrocatalysis. *Chem Rev* **2022**, *122*, 17028.

TOC Graphic

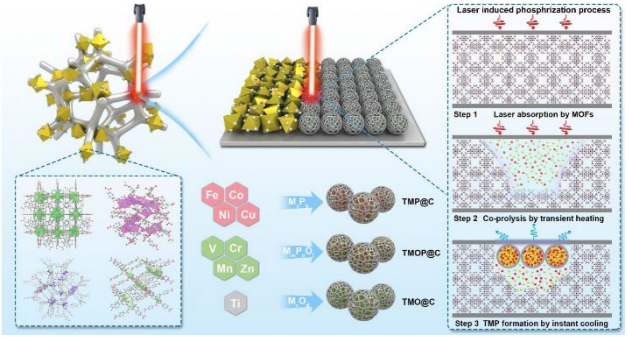
Laser induced phosphrization process
Step 1 Laser absorption by MOFs
Step 2 Co-prolysis by transient heating
Step 3 TMP formation by instant cooling
Fe
Co
Ni
Cu
V
Cr
Mn
Zn
Ti
M_P
M_P_O
M_O
TMP@C
TMOP@C
TMO@C